IVYSPRING
INTERNATIONAL PUBLISHER

Theranostics

Research Paper

Gold nanoparticles that target degraded elastin improve imaging and rupture prediction in an AngII mediated mouse model of abdominal aortic aneurysm

Xiaoying Wang[1], Brooks A Lane[2], John F Eberth[2], Susan M. Lessner[2], Naren R. Vyavahare[1]✉

1. Department of Bioengineering, Clemson University
2. Cell Biology & Anatomy, University of South Carolina School of Medicine

✉ Corresponding author: Naren Vyavahare, Ph.D., Department of Bioengineering, Clemson University, 501 Rhodes Engineering Research Center, Clemson, South Carolina, 29634; Fax number: 864-656-4466; Telephone number: 864-656-5558; Email: narenv@clemson.edu

Abstract

Background: Abdominal aortic aneurysms (AAA) are characterized by a progressive disruption and weakening of the extracellular matrix (ECM) leading to dilation of the aorta which can be fatal if not treated. Current diagnostic imaging modalities provides little insight on the varying degree of ECM degeneration that precedes rupture in AAAs. Targeted delivery of contrast agents such as gold nanoparticles (GNPs) that bind to degraded matrix could prove useful when combined with computed tomography (CT) to provide a non-invasive surrogate marker of AAA rupture potential.

Methods: AAAs were induced by chronic infusion of angiotensin II (AngII) into low density-lipoprotein receptor-deficient (LDLr -/-) mice in combination with a high-fat diet. Abdominal ultrasound was used to monitor disease progression and to assess the circumferential strain throughout the cardiac cycle. At six weeks, GNPs conjugated with an elastin antibody (EL-GNP) were injected retro-orbitally. Mice were euthanized 24 hours after EL-GNP injection, and aortas were explanted and scanned *ex-vivo* with a micro-CT system. Histological assessment and 3D models of the aneurysms with micro-CT were used to determine the EL-GNPs distribution. Isolated vessel burst pressure testing was performed on each aneurysmal aorta to quantify rupture strength and to assess rupture location.

Results: Aneurysms were found along the suprarenal aorta in AngII infused mice. Darkfield microscopy indicated EL-GNPs accumulation around the site of degraded elastin while avoiding the healthy and intact elastin fibers. Using nonlinear regression, the micro-CT signal intensity of EL-GNPs along the suprarenal aortas correlated strongly with burst pressures ($R^2=0.9415$) but not the dilation as assessed by ultrasound measurements.

Conclusions: Using an established mouse model of AAA, we successfully demonstrated *in vivo* targeting of EL-GNPs to damaged aortic elastin and correlated micro-CT-based signal intensities with burst pressures. Thus, we show that this novel targeting technique can be used as a diagnostic tool to predict the degree of elastin damage and therefore rupture potential in AAAs better than the extent of dilation.

Key words: Abdominal aortic aneurysm, gold nanoparticles, micro-CT, rupture potential

Introduction

Abdominal aortic aneurysms (AAA) are characterized by a focal dilation of the abdominal aorta due to indiscriminate vascular wall degeneration and cellular dysfunction [1]. While often asymptomatic, many aneurysms can quickly progress to rupture and fatality [2]. Those at high risk of

rupture require surgical intervention, but such procedures also include inherent perioperative risks [3]. Overall, AAA is the 14th leading cause of death in the US and one of the top 10 causes among older men [2, 4]. Although many factors contribute to the initiation of AAAs, disease onset is typically associated with extracellular matrix (ECM) degradation, primarily elastic lamina degradation by proteolytic enzymes such as matrix metalloproteinases (MMPs) and cathepsins, which are produced by activated vascular cells and infiltrating inflammatory cells [5].

The potential risk of an aneurysm rupture is determined by factors such as evolving geometry, mechanical properties, hemodynamic loads, and perivascular conditions [6]. However; clinical interventional criteria are primarily based on geometrical information such as the diameter or rate of growth of the aneurysm. This information is provided by abdominal ultrasound imaging or contrast-enhanced computed tomography (CT). Generally, open or endovascular aortic aneurysm repair is performed when the bulge diameter of an AAA increases to more than 5.5 cm as the benefits of surgery outweigh the risk involved in these procedures [7]. Although large AAAs are statistically more prone to rupture, small AAAs can fail prior to meeting the surgical criteria [4]. Patients with smaller AAAs are under a life-threatening situation since about 13% of AAAs cause death in patients before they are recommended for surgery [8]. Therefore, diameter alone is insufficient as a universal predictor for AAA failure. Identification of localized vulnerabilities (i.e., weak points within the wall) would provide crucial diagnostic information to aid clinical strategies and decrease mortality in patients suffering from AAAs.

Contrast-enhanced CT, an anatomical imaging technique, has been widely used in the diagnosis and long-term follow-up due to its ability of providing precise anatomical and morphological measurements of the AAAs [9, 10]. However, contrast-enhanced CT is unable to provide pathological information of the AAAs such as the extent of ECM degradation and identify rupture-prone AAAs accurately. Moreover, a large dose of iodine- or gadolinium-based contrast agent is required for performing contrast-enhance CT, the toxicity of which place it at a disadvantage comparing to other imaging method such as magnetic resonance imaging (MRI), nuclear imaging, and optical imaging [10, 11]. Gold nanoparticles (GNPs) have been investigated for many years as an ideal radiopaque CT contrast agent for its high density, high atomic number, high X-ray absorption coefficient and low toxicity [11]. PEGylated GNPs with

prolonged blood circulation times were used for imaging of the cardiovascular system [12]. A targeted delivery of surface modified GNPs can reduce the dose of contrast agent applied, increase the imaging quality, and provide more information of the AAAs depending on the molecular probe attached to the GNP surface. We show in this manuscript that systemic delivery of GNPs that bind to degraded elastin in an angiotensin II (AngII) mouse model of AAA provides a unique way to visualize local areas of ECM degradation that are more prone to rupture.

Methods

Preparation of anti-elastin antibody conjugated gold nanoparticles (EL-GNPs)

Citrate-capped gold nanoparticles (GNPs) were purchased from Meliorum Technologies, Rochester, NY) with an average size of 150±25nm. A heterobifunctional thiol-PEG-acid (SH-PEG-COOH) (2000MW, Nanocs, New York, NY) was added to the GNPs at a weight ratio of 4:1 and the mixture was incubated at 4°C for 48 hrs. with gentle rocking to achieve PEGylation. PEGylated GNPs were collected after centrifuging at 10,000 rpm for 20 minutes at 25 °C and resuspended in 0.1M 2-(N-morpho-lino)ethanesulfonic acid (MES) buffer (pH 5.5). EDC/NHS chemistry was followed to conjugate the PEGylated GNPs with the anti-elastin antibody. Briefly, EDC (N-(3-Dimethylaminopropyl)-N-ethyl carbodiimide hydrochloride) (Oakwood Chemical, Estill, SC)and Sulfo-NHS (N-hydroxysulfosuccini-mide) (Sigma Aldrich, St. Louis, MO) were added at a weight ratio of 2:1 and 4:1 separately to the PEGylated GNPs. This mixture was incubated at 25 °C for 6 hours with gentle vortexing. Resulting GNPs were collected after centrifuging at 10,000 rpm for 20 minutes at 25 °C and resuspended in 1mL of phosphate-buffered saline (PBS, pH 7.8). 4µg anti-elastin antibody (custom-made at Clemson University) per mg GNPs was added, and the mixture was incubated overnight at 4 °C under slow rocking. The excess antibody was removed by centrifuging the resulting solution at 10,000 rpm for 20 minutes. EL-GNPs were resuspended in saline to a concentration of 3mg/mL for injection.

Development of aneurysms in an AngII animal model:

Fifteen male low density-lipoprotein receptor-deficient (LDLr -/-) mice (2 months of age, on a C57BL/6 background) were obtained from the Jackson Laboratory (Bar Harbor, ME). Eleven mice were used for aneurysm studies while four other mice were used as healthy age-matched controls.

Aneurysms were induced by systemic infusion of angiotensin II (AngII, Bachem Americas, Torrance, CA) in combination with a diet with saturated fat (21% wt/wt) and cholesterol (0.2% wt/wt; catalog no. TD88137; Harlan Teklad) [13]. Briefly, mice were fed with high-fat diet for one week before, and six weeks during AngII infusion. Osmotic pumps (model 2004; Alzet, Cupertino, CA) filled with AngII were implanted subcutaneously through an incision at the right back shoulder of the mice. 2% to 3% isoflurane was inhaled by the mice as anesthesia throughout the surgical process. The pumping rate for AngII was set to 1000ng/kg/min. Pumps were explanted four weeks after the implantation and mice were allowed to recover for two weeks. Disease progression was monitored with a high-frequency ultrasound machine, Fujifilm VisualSonics Vevo 2100 (Fujifilm VisualSonics, Toronto, ON, Canada), by utilizing a linear array probe (MS-550D, broadband frequency 22 MHz -55 MHz). All animal use protocols for the study were approved by the Institutional Animal Care and Use Committee (IACUC) at Clemson University.

Ultrasound analysis of AAAs

The ultrasound system was used for monitoring percent dilation and to assess the circumferential strain of the aneurysm throughout the cardiac cycle. The animals were placed in supine position on the imaging table and were maintained under anesthesia by inhaling 2% to 3% isoflurane during imaging. Heart rate and body temperature of the mice were carefully monitored during the imaging process. Sagittal and transverse images for both healthy and aneurysmal aortas were obtained in motion mode. Systolic and diastolic diameters were measured and recorded at three different regions on each aneurysm or parent vessel using the built-in ultrasound software. The diastolic-to-systolic circumferential Green-LaGrange strains were calculated assuming axial symmetry using the equation given below,

$$\text{Circumferential Strain (\%)} = (1/2)((D_{sys}/D_{dia})^2 - 1) \times 100$$

Where D_{sys} represents the inner systolic aortic diameter and D_{dia} represents the inner diastolic aortic diameter.

Micro-computed tomography (Micro-CT) study

EL-GNPs were given to the mice (n=15) as a contrast agent through a retro-orbital injection at a dosage of 10 mg/kg animal weight under 2%-3% isoflurane anesthesia. Mice were euthanized 24 hrs after the injections, and intact aortas (from ascending aorta to iliac bifurcation) were explanted. Surrounding connective tissue was cleaned before micro-CT scanning. Aortas were then immersed in corn oil and imaged (90kV, 250mAs, 300ms, 0.2mm Al filter) with a Skyscan 1176 high-performance micro-CT system (Bruker, Billerica, MA). Reconstructions were carried out using the Skyscan NRecon software based on the Feldkamp algorithm. The reconstructed images of the aortas were visualized, and the dimensions of the aneurysms measured using DataViewer and CT-Vox software. 3D maximum intensity projection (MIP) images were obtained to determine the distribution of EL-GNPs within the aortas while attenuation images were acquired to study the intensity of the signals given by both EL-GNPs and tissue. Signal intensity was further quantified using CT-An software.

Aortic burst failure testing

Burst pressure testing was performed on each suprarenal aortic segment within 24 hrs after explant to study the rupture potential and location of failure. Aortas were shipped in ethylenediaminetetraacetic acid (EDTA)-free-protease-inhibitor-cocktail on ice overnight to the University of South Carolina, Columbia, SC. Branches were ligated using 12/0 nylon suture and the aneurysm, including 1-2 mm distal and proximal to the necking region, were cannulated on shortened and roughed 26G needle tips with 7/0 silk suture and mounted to our custom-designed multi-axial murine artery mechanical testing device within an adventitial bath of PBS. The device enables temperature control, hydration, inflation and extension capabilities while recording images at 45° intervals around the circumference of the tissue. All instruments are controlled via an integrated LabVIEW code. Samples reported here were first extended to an axial stretch ratio of 1.2 and then preconditioned through slow cyclic pressurization of luminal media using a syringe pump. Then the syringe pump was set to maintain an inflation rate of 1-3 mmHg/s until bursting was observed. PBS supplemented with phenol red was used as the luminal media to provide contrast capabilities to identify burst location. During inflation, the vessels were closely monitored for signs of failure, including dissection, and the pressure and location of failure were recorded. No tissue that failed at or around the mounting suture or hardware were included in the analysis.

Morphological analysis of the explanted suprarenal abdominal aorta

Morphological analysis was performed in the suprarenal area of the abdominal aorta. Outer aortic diameters were measured on the abdominal ultrasound basic-mode-images at three different time points during a cardiac circle within the parent vessel and the lesion. Mean values were then calculated for each. The dilation was calculated using the equation given below,

$$\text{Dilation (\%)} = (\overline{D_L} - \overline{D_H})/\overline{D_L} \times 100$$

where $\overline{D_H}$ represents the mean outer diameter of the healthy portion of the aorta and $\overline{D_L}$ the mean outer diameter the pathological section.

Histological analysis of the aneurysms

Cryosections of both aneurysms and healthy aortas were used for histological analysis. Aortas were fixed in buffered formalin, embedded in optimal cutting temperature (OCT) compound (Sakura Finetek, Torrance, CA) after being washed in deionized (DI) water and sectioned per standard procedures. Five-micrometer sections were mounted on positively charged glass slides. Slides were placed in 100% pre-cooled acetone (Fisher Science Education, Nazerath, PA) for 10 minutes to adhere the tissues to the slides. Subsequently, the slides were rinsed with tap water for 3 minutes to remove the OCT compound for further staining. Slides were then stained with Verhoeff-van Gieson (VVG) to visualize the elastin damage in different samples.

Identification of EL-GNPs by darkfield microscopy and hyperspectral mapping

Cryosectioned histological samples (5µm) were examined with a CytoViva enhanced darkfield microscope optics system (CytoViva, Inc., Auburn, AL). The system (Olympus BX51) employs an immersion oil (Type A, nd> 1.515, Cargille Brand) ultra-dark-field condenser and a 40× air Plan-FL objective with an adjustable numerical aperture from 1.2 to 1.4. Illumination was provided by a Fiber-lite DC 950 regulated illuminator. Enhanced darkfield microscopy images were obtained using Exponent7 software with a gain setting of 2.8 and exposure time of 53 ms to visualize the EL-GNPs. A hyperspectral imager (mounted on a microscope and controlled by Environment for Visualization software from Exelis Visual Information Solutions, Inc.) was used to extract spectral information for mapping the EL-GNPs in the samples at an exposure time of 0.25ms with a full field of view (643 lines). Negative control samples (without GNPs) were imaged and analyzed to create a spectral library as a reference. Gold mapping was achieved by applying a filtered spectral library by subtracting the negative control spectral library.

Statistics

All the normally distributed results, including graphs in the figures, are given as mean±S.D, while the results which are not normally distributed are given as a range with median. Normality tests were performed using probability plot and chi-square tests at a significant level of 0.05%. Statistical analysis was performed using a one-way analysis of variance (ANOVA) and Tukey's HSD as a post-hoc test. Results were considered significantly different when p-values ≤0.05. Non-linear regression was performed using a power model and regression coefficients were calculated for each model.

Results

Characterization of EL-GNPs

EL-GNPs were prepared by conjugating the custom-made antibody that recognizes degraded elastin with commercial gold nanoparticles (GNPs). They were characterized by a particle size analyzer for size and surface charge before and after the conjugation process. Before antibody conjugation, bare GNPs had an average size of 150±25nm and a Zeta potential of -29.2±3.91mv. EL-GNPs had a final average size of 184.2±18.09nm. The zeta potential of the NPs was measured as -5.06±1.25mv.

Systemic AngII infusion-induced aneurysm mouse model

A flow chart for animal experimentation is shown in Figure 1. Severe aortic dilation (> 1.5-fold) was observed at the suprarenal abdominal aorta in 9 out of 11 mice and moderate enlargement in the remaining two AngII-infused mice (Figure 2A). 2D transverse micro-CT images revealed an increase of aortic outer diameters and thickening of aortic wall in the lesions compared to the normal aorta (Figure 2B). The enlargement of the suprarenal aortic diameters resulting from the systemic infusion of AngII varied from 12.18%-144.83% of the normal size (Table S1). VVG staining of the aneurysmal aorta demonstrated the degradation of elastin laminae inside the aortic wall. Aneurysm development in mice corresponded with the extent of elastic lamina degradation (Figure 2C).

EL-GNPs targeting to degraded elastin in the damaged aorta

3D reconstructed attenuation micro-CT models of the explanted aortas presented much higher concentration of EL-GNPs at the aneurysmal area indicating they targeted the aneurysmal aortic sites within 24 hours while sparing the healthy regions of the aorta (Figure 3A). Enhanced darkfield microscopy (EDFM) in combination with VVG staining further confirmed the targeting of EL-GNPs within the aneurysmal tissues. EL-GNPs were found in darkfield microscopy images (Figure 3B) accumulating exclusively around the degraded elastin as identified by VVG staining while sparing healthy and intact elastin fibers (Figure 3C).
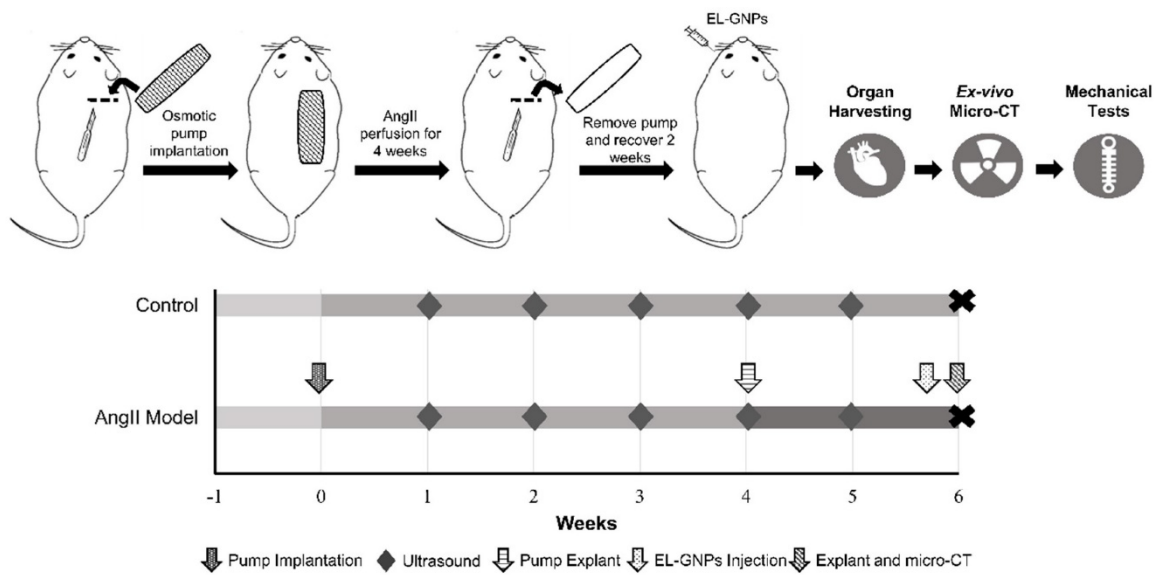
Figure 1. Schematic representation of the study design. Two study groups were used in this study. For the angiotensin II infused group, mice were fed with a high fat diet for 1 week before implantation of angiotensin II-filled osmotic pump. Osmotic pumps were explanted 4 weeks later. For the control group, mice were fed with chow diet and no pump was implanted. Gold nanoparticles were injected retro-orbitally to both groups by the end of 6th week after osmotic pump implantation. At the end of the experiment, animals were euthanized and organs were harvested for ex-vivo micro computed tomography scans and mechanical tests.
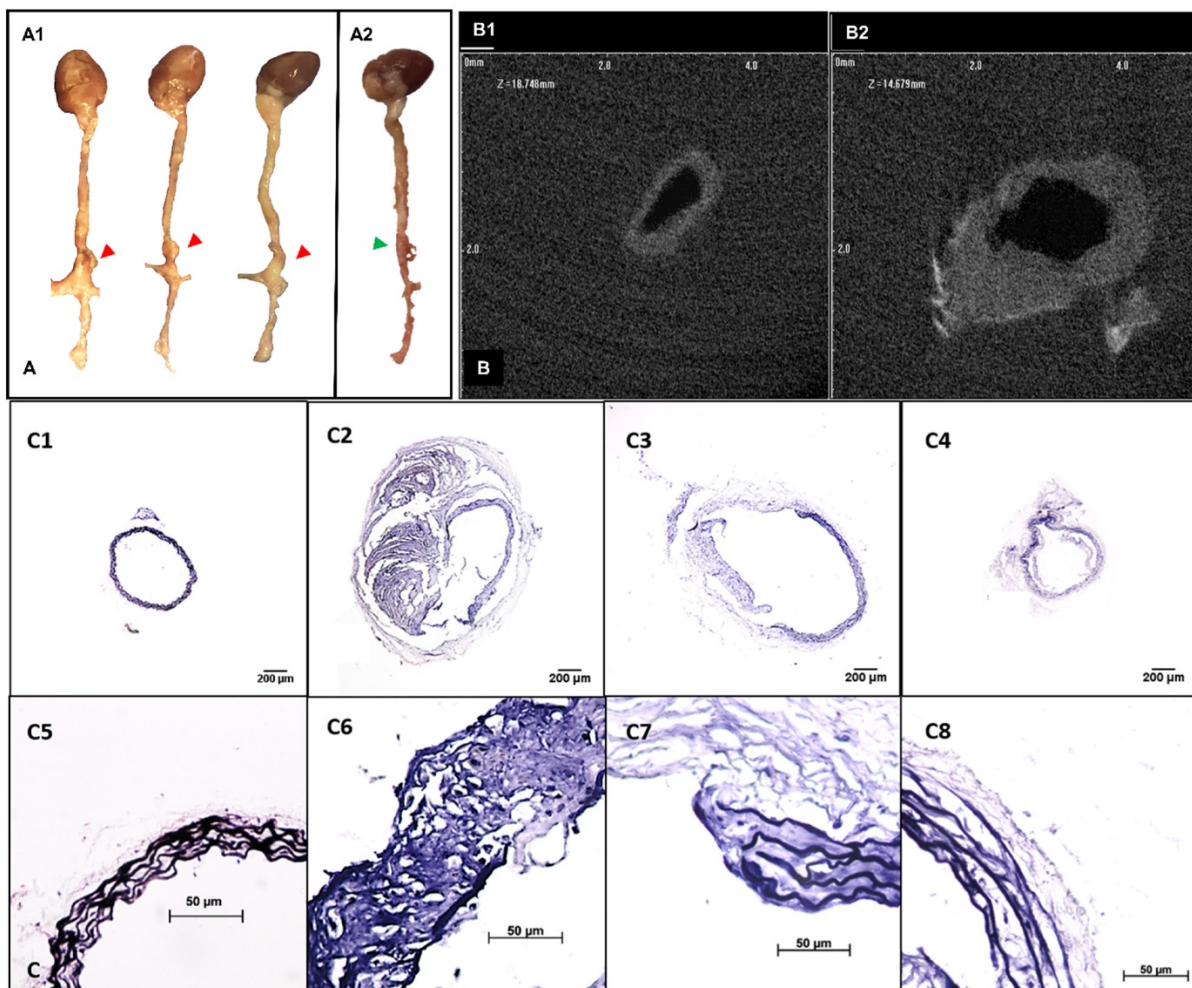

Figure 2. Development of suprarenal aortic aneurysms with various properties. A. Representative pictures showing the morphology of the whole explanted aortas. Visible dilations (indicated by red arrows) were found at the suprarenal abdominal aortic regions in most of the angiotensin II pump-implanted mice (A1, n=10) while one had no visible dilation (A2). **B.** Ex-vivo micro computed tomography image showing the cross-sections of aortas at the healthy region (C1) and the aneurysmal region (C2). Aneurysmal aortas presented a thickened vessel wall on the anterior side and an increase in diameter compared to the healthy vessel. **C.** Verhoeff-van Gieson staining shows different levels of elastin degradation amongst aneurysmal tissues (4x, C2-C4, 40x, C6-C8) compared to the healthy aortic control with only intact elastin (4x, C1, 40x, C5). Scale bar =200µm for 4x images (C1-C4). Scale bar =50µm for 40x images (C5-C8).
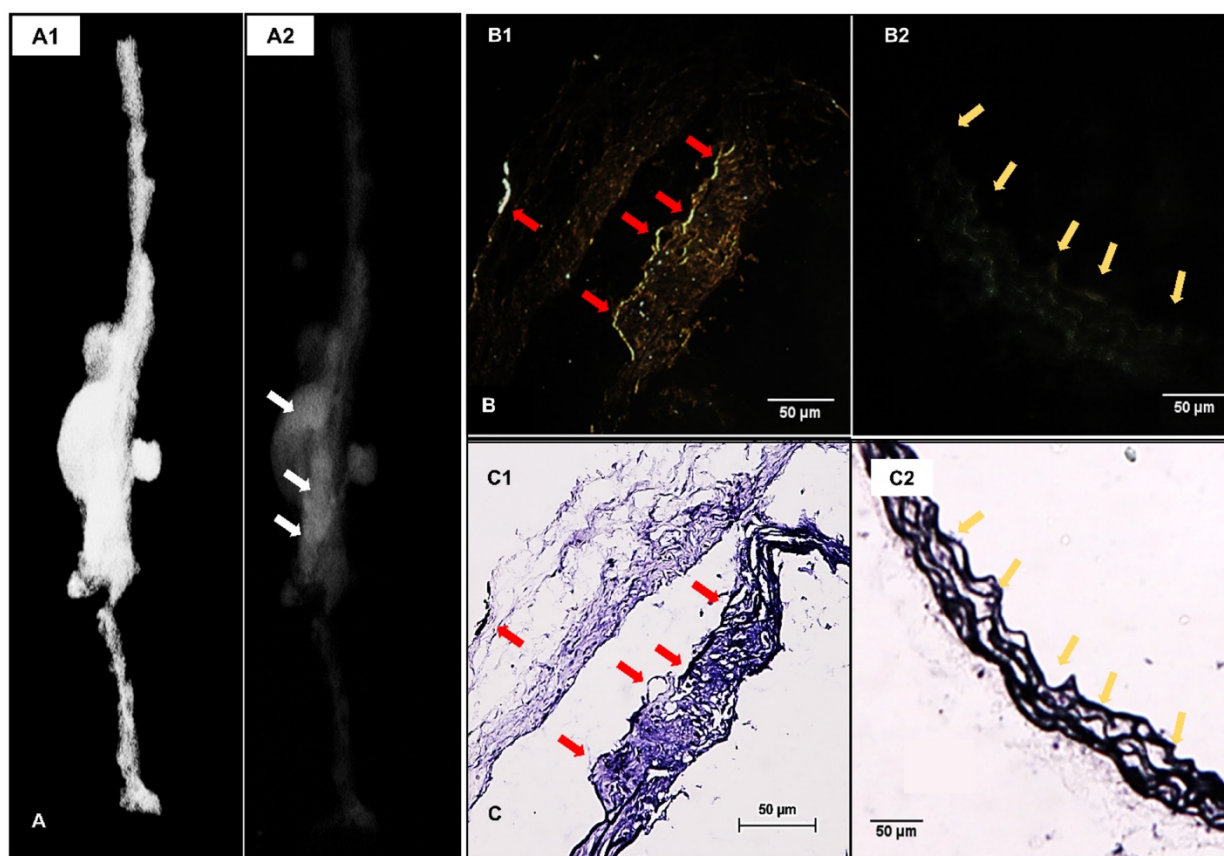
Figure 3. Localization of EL-GNPs within aneurysmal tissues. A. 3D model that visualizes the explant morphology of an aneurysmal aorta (A1) and attenuation mode that shows the distribution of degraded elastin targeting gold nanoparticles within the whole aorta (A2). A stronger signal was shown in the aneurysmal aortic segment than the healthy aortic segment. **B.** Enhanced dark field microscopy and **C.** histological analysis of elastin with Verhoeff van Gieson staining. A stronger darkfield microscopy signal was found in the section (B1) which showed more elastin damage (C1) than the control section (B2) that contained only intact elastin fibers (C2). Signal given by gold nanoparticles was found at the positions where degraded elastin was present, indicated by red arrows, while healthy and intact elastin fibers were devoid of signal as indicated by yellow arrows. Scale bar =50μm.

EL-GNP accumulation indicates elastin damage level

Hyperspectral imaging (HSI), in conjunction with EDFM, provided spectral information for the aneurysms with bound EL-GNPs. Specific signatures of EL-GNPs were mapped and separated from the noise given by the tissue according to their different spectral features. Bright field microscopy indicated different levels of elastin damage within different tissue samples by VVG staining (Figure 4A). EDFM and hyperspectral mapping corresponding to the regions visualized in bright field microscopy demonstrated that the amount of EL-GNPs that accumulated within the tissue samples varied with the elastin damage level (Figure 4B, 4C, 4D). Decreasing integrity of elastin fibers in the aortic wall increased EL-GNP accumulation. When extensive damage to elastin laminae was present in the bright field image (Figure 4A2), hyperspectral mapping identified a large quantity of EL-GNPs in the tissue (Figure 4D2). Conversely, no EL-GNP accumulation was mapped (Figure 4D1) in a control sample that showed no signs of elastin degradation (Figure 4A1).

Ultrasound analysis of AAAs

Ultrasound images of abdominal aortas were obtained prior to euthanasia. Healthy controls exhibited a relatively uniform inner diameter (Figure 5A1) while dilation in the AngII infused mice was most commonly observed at the suprarenal location (Figure 5A2-A4). Circumferential strains for all eleven samples ranged from 4.28 to 12.82% (Figure S1). Circumferential strains of the healthy aortas were 16.08±2.40% (n=3) and were significantly decreased at the aneurysmal aortic regions of the AngII-infused mice to (Figure 5B). For aneurysms with a similar extent of dilation (MS#1, #5 and #11, 92% dilation,), the circumferential strains were 4.28±1.17%, 5.95±1.08% and 9.60±1.05% respectively, suggesting the acute distensibility of the aneurysmal aortic wall was not necessarily related to the extent of chronic dilation (Figure 5B).

Correlation of rupture risk parameters and burst pressure of the aorta

The burst pressures for the samples harvested from AngII-infused mice varied from 141 to 540

mmHg, while the burst pressure range for healthy aortic controls was from 545 to 588mmHg, with a median of 566.5mmHg. The 3D micro-CT models of the aortas showed higher signal intensity at the suprarenal aortic regions of specimens having lower burst pressures, indicating that the accumulation of our EL-GNPs was inversely correlated to the load at failure (Figure 6A1-6A3) while the age-matched control samples did not show any signs of EL-GNPs accumulation (Figure 6A4). In order to establish a quantitative relationship between the signal and the ultimate burst pressure of the suprarenal aortas, the signals of the healthy aortic regions were used as negative controls and were subtracted from the total.

For the age-matched control groups, the signal strength for all samples in the suprarenal region was 0. As the burst pressures of the suprarenal aorta decreased, indicating a weakening of the aorta, higher signals for EL-GNPs were detected (Figure 6B). A power-law equation $y = 20+08x^{-3.586}$ was established with $R^2=0.9415$, where x represents the burst pressure and y represents the signal intensity, which demonstrated that the signal strengths given by EL-GNPs had a strong negative correlation to the burst pressures of the aneurysmal tissues (Figure 6B1) whereas changes in aortic dilation ($R^2=0.1932$) or circumferential strain ($R^2=0.3918$) failed to show strong correlations to burst pressures (Figure 6C, 6D).
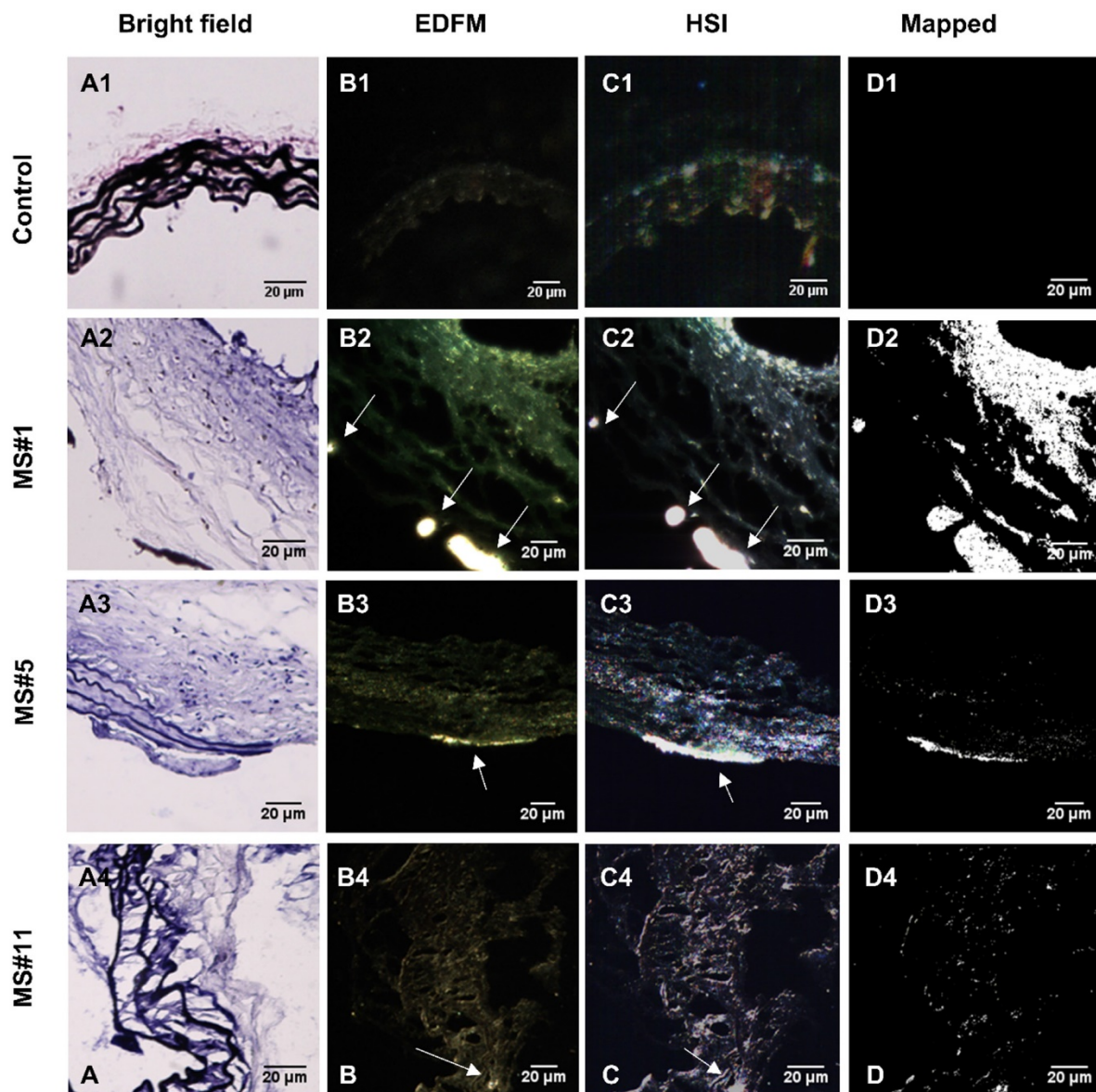

Figure 4. Hyperspectral mapping of suprarenal aorta tissue targeted by EL-GNPs. Rows from top to bottom correspond to suprarenal aortas with different levels of elastin damage within the aortic walls, from high to low, respectively. **A.** Brightfield microscopy images (40X) after Verhoeff-van Gieson staining demonstrated different elastin degradation levels in the selected tissue samples; **B.** Enhanced darkfield microscopy (EDFM, 40X) showed the existence of high contrast degraded elastin targeting gold nanoparticles in the tissues denoted by the white arrows; **C.** Hyperspectral images (HSI, 40X) and **D.** hyperspectral images mapped (Mapped) against their respective reference spectrum library as generated with negative controls. These identified a more extensive distribution of degraded elastin targeting gold nanoparticles compared to darkfield microscopy images. Mapped degraded elastin targeting gold nanoparticles quantity increased with elastin damage as shown in the Verhoeff-van Gieson -stain sections. Scale bar =20µm.
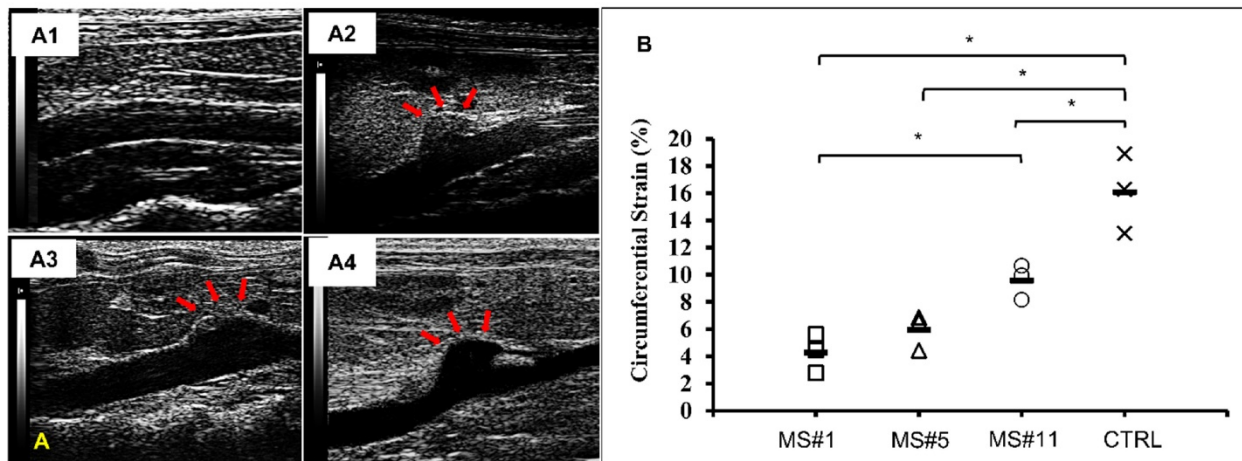
Figure 5. *In vivo* **ultrasound and circumferential strains. A.** Representative B-mode in vivo ultrasound images of abdominal aortas before euthanasia of the MS#1 (A1), MS#5 (A2) and MS#11(A3) showing focalized aortic dilation indicated by red arrows. **B.** Corresponding circumferential Green-LaGrange strains throughout the cardiac cycle. All aneurysmal aortas showed a reduction in the strain values when compared to a healthy control. These three aneurysmal samples were selected due to similar dilations (92%) but with different degrees of elastin damage. Ms#11 had minor aortic elastin damage and Ms#1 had severe aortic elastin damage. * (One-way ANOVA with Tukey's HSD) represents statistical significance (P<0.05). Solid line in each group represents the mean value.
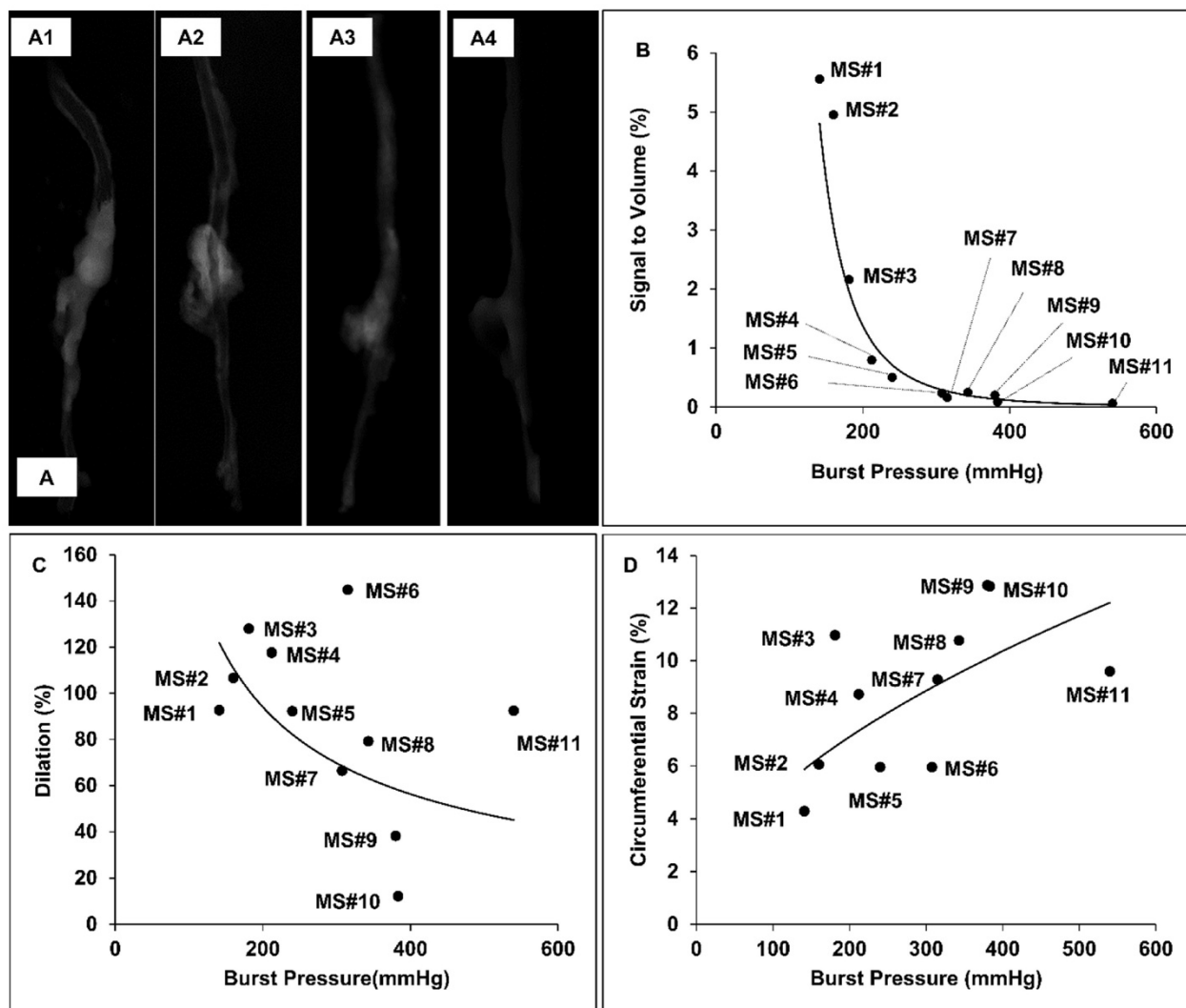

Figure 6. Representative reconstructed aorta models in attenuation mode and correlation between signal intensity, diameter increase and burst pressure. A. 3D aorta models were reconstructed in attenuation mode for MS#1 (A1), MS#5 (A2), MS#11(A3) and control mouse (A4). The signal intensity shown in the suprarenal aortic segments decreases as elastin damage decreases. **B.** A strong negative nonlinear correlation between signal intensity and burst pressure was found using the power model (R^2=0.9415, y = 20+08x$^{-3.586}$), while **C.** dilation vs. burst pressure and **D.** the circumferential Green-LaGrange strains vs. burst pressure were only weakly correlated with each other using the power-law, suggesting that the signal intensity induced by the accumulated degraded elastin targeting gold nanoparticles could serve as a better parameter to predict rupture potential than dilation.
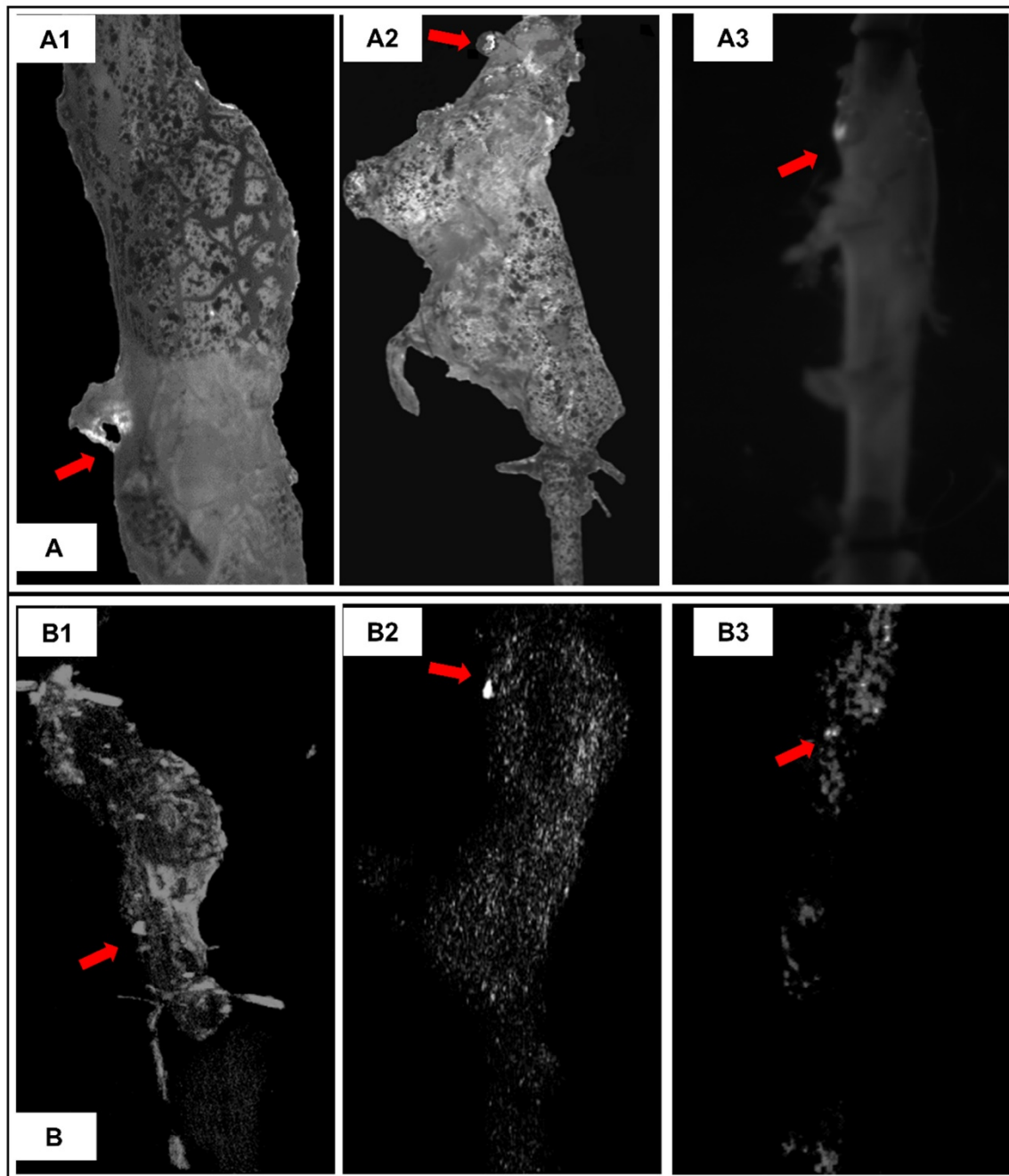
Figure 7. Representative burst pressure tests pictures and corresponding reconstructed aorta models in maximum intensity projection (MIP) mode. A. Burst pressure test pictures for MS#2 (A1), MS#3 (A2) and MS#7 (A3) showing the location on the aneurysmal wall where rupture is initiated under pressurization. **B.** For corresponding mouse aorta, the degraded elastin targeting gold nanoparticles induced signals in the reconstructed 3D aortic models using maximum intensity projection mode were non-uniformly distributed within the aneurysmal segments. High-intensity spots correlate to the rupture sites, indicating that accumulation of degraded elastin targeting gold nanoparticles within the aneurysm could be used to predict the weak site of the aneurysm.

EL-GNP distribution and the initial burst site within the suprarenal aortas

The initial site where suprarenal aortas started to rupture under pressurization were captured by a camera through visualization of the PBS supplemented with phenol red being expelled at rupture site (Figure 7A arrows). 3D micro-CT data was displayed in a maximum intensity projection (MIP) mode, in which the lower-attenuation structures are not well visualized [14], in order to study the distribution of EL-GNPs within the aneurysmal region (Figure 7B). Bright spots for EL-GNPs were seen where the first rupture occurred, suggesting that the weakest spots had the highest GNP signal.

Discussion

This study aims to develop a potential targeted contrast agent for CT imaging which will provide

morphological information along with a better assessment of the rupture risk of AAAs. Nanoparticles have been used for the development of enhanced molecular imaging technologies targeting cancer cells [15]. GNPs are commonly used due to their outstanding properties such as noncytotoxicity, excellent biocompatibility, ease of surface functionalization, strong light absorption and scattering effects [15, 16]. Gehrmann *et al.* reported using 50nm cmHsp70.1-conjugated GNPs for imaging Hsp70 membrane-positive mouse tumor cells in vivo [17]. In this study, we used spherical gold nanoparticles with a diameter of around 180 nm to target the AAAs. The increase in gold particle size from ~150nm to ~180nm after the antibody conjugation process indicated that we successfully conjugated the elastin antibody to the surface of the gold nanoparticles to achieve targeted delivery. Moreover, we optimized the conjugation process in order to achieve targeting while ensuring the high image quality (Figure S2).

Suprarenal aortic aneurysms were successfully initiated by systemically delivering AngII into LDLr -/- genetic background mice. AAAs were considered significant when the dilation of the aorta exceeded 1.5 times (i.e., 50% dilation) its normal external diameter [18]. Based on this criterion, the AAA incidence for our study was 81.82%, which is higher than the 56% incidence rate of AAAs in AngII infused mice reported by Trachet *et al.* [19]. This may be due to an extended 42-day-aneurysm-progression process instead of the commonly described 28 days [13]. Pathological features such as degradation of the elastic lamina and atherosclerosis were demonstrated by the histological study results. These features are consistent with what has been reported in the AngII infusion-induced AAA in the ApoE-/- genetic background mouse model [20], as well as in human AAAs [2]. However, our results showed that the diameter increase, elastin degradation level, and intraluminal atherosclerotic plaque formation of the suprarenal aortas vary among animals. In fact, two samples did not meet the 1.5-fold threshold (MS#9 an Ms#10; Table S1) but still presented with elastin damage (Figure S3). Such variability was advantageous in this study because it enabled a wider spectrum fragmentation for correlation with GNP accumulation.

To date, the targeting of AAAs for therapeutic and imaging purposes remains significantly challenging because of the limited number of viable targets and a relatively low hemodynamic residence time and limited viable targets in the diseased aorta. Key pathological processes occurring within AAAs such as inflammation, vascular smooth muscle cell apoptosis, and even ECM remodeling have emerged as potential targets for nanoparticle-based diagnostics [21]. Shirasu *et al.* reported a passive AAA targeting system using rapamycin nanoparticles. Although the mechanism for this system was not fully understood, they hypothesized that the accumulation of nanoparticles was a result of micro-defects caused by inflammatory cell infiltration and ECM fragmentation [22]. For active targeting, macrophage targeting was reported for an MRI imaging with ultra-small superparamagnetic iron oxide (USPIO) and fluorine 18-labeled cross-linked iron oxide (^{18}F-CLOF) in AngII-induced AAA using an ApoE -/- mouse model [23-25]. Klink *et al.* [26] described the targeting of aortic adventitial ECM remodeling-related collagen in AngII-infused and TGFβ-neutralized C57BL/6 mice using paramagnetic/fluorescent micellar nanoparticles functionalized with a collagen-binding protein (CNA-35). All these previous targeting efforts focused on either inflammatory cells or collagen. Levels of inflammation and collagen remodeling vary with time and therefore cannot be used as a reliable surrogate for chronic aneurysmal rupture risk assessment.

On the other hand, the adult elastic lamina does not remodel substantially within the timeline of aortic disease progression and the degradation of in the aneurysmal wall is a consistent feature of AAAs making it an ideal target for delivering nanoparticles. In our study, we successfully targeted gold nanoparticles to the aneurysmal site in AngII-infused LDLr (-/-) mice by conjugating them with antibodies that target only degraded-elastin as described previously [27]. Our results suggested that the targeting of our EL-GNPs was both elastin-specific and damage-dependent as most of the EL-GNPs were found attached to degraded elastin while the healthy aorta showed minimal EL-GNPs attachment. Furthermore, the quantity of EL-GNPs accumulated in the aneurysmal tissue was related to the extent of local elastin degradation which highlights altered biomechanical properties of the aortic wall leading to further disease progression and failure [28]. Thus, we tested if EL-GNPs targeting could improve imaging and could be used as a potential non-invasive AAA rupture risk stratification tool.

Non-invasive abdominal ultrasound is commonly used in diagnosis and monitoring of AAAs, mainly providing morphological information to evaluate disease progression. Others reported that high-frequency ultrasound could be used to assess aortic wall strain as part of a biomechanical analysis in murine models [29, 30]. Our *in-vivo* abdominal ultrasound results indicated a reduction of circumferential wall strain throughout the cardiac

cycle in the aneurysmal suprarenal aorta compared to the healthy aorta and these findings are consistent with the results from previous studies. We also found that the amount of EL-GNPs accumulated increased with decreasing wall strain. Our results demonstrate that there could be a correlation between EL-GNP accumulation and overall biomechanics of the aneurysmal tissue.

Burst testing, a direct method of identifying rupture pressure and location, supported the correlation between the signal given by targeted EL-GNP signal and the rupture potential of aneurysms [31]. Using a power model, a strong negative correlation was found between EL-GNPs and the pressures at which a AAA will burst. Since aortic diameter is the primary clinical criteria used for surgical intervention it was interesting to note that no immediate pattern emerged correlating burst pressure to the extent of dilation in our AAAs. Although many large AAAs failed at lower pressures, others withstood much higher pressures. Incidentally, most AAAs in our study failed at or around the necking region and a few failed at the site of the branches. Likewise, aneurysms with similar dilation were shown to experience varying levels of circumferential strain throughout the cardiac cycle. Thus, the signal intensity of EL-GNPs measured by CT shows a more meaningful relationship with the rupture risk of AAAs than does the increase in diameter or a decrease in circumferential strain.

The variability of the animal model used in the current work provides a tremendous strength in assessing our micro CT-based EL-GNPs approach to AAA rupture potential. Variations in EL-GNP distribution were found not only among different suprarenal aortic segments but also within the same aorta, suggesting variable degrees of elastin damage within the aneurysm and the possible existence of a 'weak point' where the rupture of the aneurysm initiates. Thus, our data suggests that an extent ECM degradation visualized using our EL-GNP contrast could be a more meaningful way to look at which patients are more prone to rupture and need immediate attention.

Conclusions

An AngII infusion LDLr -/- mouse model provided us with AAAs at different stages and having different biological and biomechanical properties. Degradation of elastin led to a decrease in aortic wall strain and a decrease in burst pressures in the aneurysmal aorta. EL-GNPs enabled visualization of the degraded elastin in AAA sites so that the quantity of GNPs could be used as a marker to predict the rupture risk and rupture sites for AAAs. This approach is highly advantageous because small and pre-aneurysmal tissues would likely demonstrate elastin damage prior to ultrasound diagnostics. Thus, such degraded elastin-targeting nanoparticles have the diagnostic potential as a sensitive noninvasive AAA targeting contrast agent for CT imaging.

Limitations of this study: We have used a well-established AngII model to assess AAAs. Aneurysms in this model, however, do not spontaneously rupture, so all burst pressure testing was performed on explanted aortas for correlation of rupture risk. Also, micro-CT data was obtained on explanted aortas and not in situ as the signal intensity of gold NPs at the concentrations used in this study was not enough to get a contrast difference from the surrounding tissues. We have not done detailed biodistribution and clearance study for EL-GNPs as animals were sacrificed 24 hours after EL-GNP injections. We were able to locate EL-GNPs in spleen, liver, and kidneys but not in heart and lungs at the explant. Future studies will focus on using higher concentration of gold NPs for a better *in vivo* signal and detailed biodistribution and clearance of GNPs.

Abbreviations

AAA: abdominal aortic aneurysms; AngII: angiotensin II; ANOVA: Analysis of variance; ApoE-/-: Apolipoprotein E deficient; CT: computed tomography; DI: deionized; ECM: extracellular matrix; EDC: N-(3-Dimethylaminopropyl)-N-ethyl carbodiimide hydrochloride; EDFM: enhanced dark field microscopy; EDTA: ethylenediaminetetraacetic acid; EL-GNP: elastin antibody conjugated gold nanoparticle; 18F-CLOF: fluorine 18-labeled cross-linked iron oxide; GNP: gold nanoparticles; HIS: hyperspectral imaging; IACUC: institutional animal care and use committee; LDLr-/-: low density lipoprotein receptor deficient; MES: 2-(N-morpholino)ethanesulfonic acid; MIP: maximum intensity projection; MMP: matrix metalloproteinase; MS: mouse; OCT: optimal cutting temperature; PBS: phosphate buffered saline; Sulfo-NHS: N-hydroxysulfosuccinimide; USPIO: ultra-small superparamagnetic iron oxide; VVG: Verhoeff-van Gieson stain.

Supplementary Material

Supplementary figures and table.
http://www.thno.org/v09p4156s1.pdf

Imaging Facility for their help with darkfield microscopy.

Competing Interests

NRV holds significant equity in Elastrin Therapeutics Inc., which has licensed this technology from Clemson University.

References

1. Kuivaniemi H, Ryer EJ, Elmore JR, Tromp G. Understanding the pathogenesis of abdominal aortic aneurysms. Expert Rev Cardiovas. 2015; 13: 975-87.
2. Aggarwal S, Qamar A, Sharma V, Sharma A. Abdominal aortic aneurysm: A comprehensive review. Exp Clin Cardiol. 2011; 16: 11-5.
3. Siracuse JJ, Gill HL, Graham AR, Schneider DB, Connolly PH, Sedrakyan A, et al. Comparative safety of endovascular and open surgical repair of abdominal aortic aneurysms in low-risk male patients. Journal of Vascular Surgery. 2014; 60: 1154-8.
4. Isenburg JC, Simionescu DT, Starcher BC, Vyavahare NR. Elastin stabilization for treatment of abdominal aortic aneurysms. Circulation. 2007; 115: 1729-37.
5. Thompson RW, Holmes DR, Mertens RA, Liao S, Botney MD, Mecham RP, et al. Production and localization of 92-kilodalton gelatinase in abdominal aortic aneurysms. An elastolytic metalloproteinase expressed by aneurysm-infiltrating macrophages. J Clin Invest. 1995; 96: 318-26.
6. Humphrey JD, Holzapfel GA. Mechanics, mechanobiology, and modeling of human abdominal aorta and aneurysms. J Biomech. 2012; 45: 805-14.
7. LeFevre ML, Force USPST. Screening for abdominal aortic aneurysm: U.S. Preventive Services Task Force recommendation statement. Ann Intern Med. 2014; 161: 281-90.
8. Vorp DA. Biomechanics of abdominal aortic aneurysm. J Biomech. 2007; 40: 1887-902.
9. Sparks AR, Johnson PL, Meyer MC. Imaging of abdominal aortic aneurysms. Am Fam Physician. 2002; 65: 1565-70.
10. Hong H, Yang YA, Liu B, Cai WB. Imaging of Abdominal Aortic Aneurysm: The Present and the Future. Curr Vasc Pharmacol. 2010; 8: 808-19.
11. Lusic H, Grinstaff MW. X-ray-Computed Tomography Contrast Agents. Chem Rev. 2013; 113: 1641-66.
12. Kim D, Park S, Lee JH, Jeong YY, Jon S. Antibiofouling polymer-coated gold nanoparticles as a contrast agent for in vivo X-ray computed tomography imaging (vol 129, pg 7661, 2007). J Am Chem Soc. 2007; 129: 12585-.
13. Cassis LA, Gupte M, Thayer S, Zhang X, Charnigo R, Howatt DA, et al. ANG II infusion promotes abdominal aortic aneurysms independent of increased blood pressure in hypercholesterolemic mice. Am J Physiol Heart Circ Physiol. 2009; 296: H1660-5.
14. Perandini S, Faccioli N, Zaccarella A, Re T, Mucelli RP. The diagnostic contribution of CT volumetric rendering techniques in routine practice. The Indian journal of radiology & imaging. 2010; 20: 92-7.
15. Gao J, Huang XY, Liu H, Zan F, Ren JC. Colloidal Stability of Gold Nanoparticles Modified with Thiol Compounds: Bioconjugation and Application in Cancer Cell Imaging. Langmuir. 2012; 28: 4464-71.
16. Medley CD, Smith JE, Tang Z, Wu Y, Bamrungsap S, Tan W. Gold nanoparticle-based colorimetric assay for the direct detection of cancerous cells. Anal Chem. 2008; 80: 1067-72.
17. Gehrmann MK, Kimm MA, Stangl S, Schmid TE, Noel PB, Rummeny EJ, et al. Imaging of Hsp70-positive tumors with cmHsp70.1 antibody-conjugated gold nanoparticles. Int J Nanomedicine. 2015; 10: 5687-700.
18. Kontopodis N, Pantidis D, Dedes A, Daskalakis N, Ioannou CV. The - Not So - Solid 5.5 cm Threshold for Abdominal Aortic Aneurysm Repair: Facts, Misinterpretations, and Future Directions. Front Surg. 2016; 3: 1.
19. Trachet B, Fraga-Silva RA, Jacquet PA, Stergiopulos N, Segers P. Incidence, severity, mortality, and confounding factors for dissecting AAA detection in angiotensin II-infused mice: a meta-analysis. Cardiovasc Res. 2015; 108: 159-70.
20. Lysgaard Poulsen J, Stubbe J, Lindholt JS. Animal Models Used to Explore Abdominal Aneurysms: A Systematic Review. Eur J Vasc Endovasc Surg. 2016; 52: 487-99.
21. Emeto TI, Alele FO, Smith AM, Smith FM, Dougan T, Golledge J. Use of Nanoparticles As Contrast Agents for the Functional and Molecular Imaging of Abdominal Aortic Aneurysm. Front Cardiovasc Med. 2017; 4: 16.
22. Shirasu T, Koyama H, Miura Y, Hoshina K, Kataoka K, Watanabe T. Nanoparticles Effectively Target Rapamycin Delivery to Sites of Experimental Aortic Aneurysm in Rats. PLoS One. 2016; 11: e0157813.
23. Nahrendorf M, Keliher E, Marinelli B, Leuschner F, Robbins CS, Gerszten RE, et al. Detection of macrophages in aortic aneurysms by nanoparticle positron emission tomography-computed tomography. Arterioscler Thromb Vasc Biol. 2011; 31: 750-7.
24. Yao Y, Wang Y, Zhang Y, Li Y, Sheng Z, Wen S, et al. In vivo imaging of macrophages during the early-stages of abdominal aortic aneurysm using high resolution MRI in ApoE mice. PLoS One. 2012; 7: e33523.
25. Turner GH, Olzinski AR, Bernard RE, Aravindhan K, Boyle RJ, Newman MJ, et al. Assessment of macrophage infiltration in a murine model of abdominal aortic aneurysm. J Magn Reson Imaging. 2009; 30: 455-60.
26. Klink A, Heynens J, Herranz B, Lobatto ME, Arias T, Sanders HM, et al. In vivo characterization of a new abdominal aortic aneurysm mouse model with conventional and molecular magnetic resonance imaging. J Am Coll Cardiol. 2011; 58: 2522-30.
27. Sinha A, Shaporev A, Nosoudi N, Lei Y, Vertegel A, Lessner S, et al. Nanoparticle targeting to diseased vasculature for imaging and therapy. Nanomedicine. 2014; 10: 1003-12.
28. Collins MJ, Eberth JF, Wilson E, Humphrey JD. Acute mechanical effects of elastase on the infrarenal mouse aorta: implications for models of aneurysms. J Biomech. 2012; 45: 660-5.
29. Goergen CJ, Barr KN, Huynh DT, Eastham-Anderson JR, Choi G, Hedehus M, et al. In vivo quantification of murine aortic cyclic strain, motion, and curvature: implications for abdominal aortic aneurysm growth. J Magn Reson Imaging. 2010; 32: 847-58.
30. Favreau JT, Nguyen BT, Gao I, Yu P, Tao M, Schneiderman J, et al. Murine ultrasound imaging for circumferential strain analyses in the angiotensin II abdominal aortic aneurysm model. J Vasc Surg. 2012; 56: 462-9.
31. Laterreur V, Ruel J, Auger FA, Vallieres K, Tremblay C, Lacroix D, et al. Comparison of the direct burst pressure and the ring tensile test methods for mechanical characterization of tissue-engineered vascular substitutes. J Mech Behav Biomed Mater. 2014; 34: 253-63.